RESEARCH ARTICLE | MARCH 09 2026

# Influence of the number of blades on the wake development of rim-driven thrusters

Antonio Posa ; Stefano Gaggero ; Riccardo Broglia



*Physics of Fluids* 38, 035127 (2026)
https://doi.org/10.1063/5.0314358

Physics of Fluids ARTICLE pubs.aip.org/aip/pof

# Influence of the number of blades on the wake development of rim-driven thrusters

Cite as: Phys. Fluids **38**, 035127 (2026); doi: 10.1063/5.0314358
Submitted: 28 November 2025 · Accepted: 9 February 2026 ·
Published Online: 9 March 2026

View Online Export Citation CrossMark

Antonio Posa,[1,a)] Stefano Gaggero,[2] and Riccardo Broglia[1]

## AFFILIATIONS

[1]CNR-INM, Institute of Marine Engineering, National Research Council of Italy, Via di Vallerano 139, 00128 Roma, Italy
[2]University of Genoa, Department of Naval Architecture, Electrical, Electronic and Telecommunication Engineering, Via Montallegro 1, 16145 Genova, Italy

[a)]Author to whom correspondence should be addressed: antonio.posa@cnr.it

## ABSTRACT

The wake systems of rim-driven thrusters (RDTs) with different numbers of blades, producing the same overall thrust, are compared by using a large eddy simulation methodology. For all cases, the shear produced at the outer boundary of the wake results in a quick breakup of the helical vortices shed at the outermost radial coordinates, while those at the innermost radii keep coherent up to the outlet section of the computational domain, located five diameters downstream of the propeller plane. The vortices within the trailing wake of each blade undergo merging into larger structures, while, in contrast with the wake development process typical of conventional propellers, no mutual inductance phenomena between the vortices shed by neighboring blades were observed, even as the number of blades increases. Therefore, more blades experiencing lower loads result in less intense vortices, shear layers, and turbulent stresses, since the decreasing azimuthal distance between trailing wakes and vortices from neighboring blades was not found to trigger more intense interactions and a faster diffusion. These results suggest that more blades are beneficial to the wake properties of RDTs, at least in the range of blade numbers considered in this study, from three to six.





## I. INTRODUCTION

Rim-driven thrusters (RDTs) are unconventional marine propellers.[1] They differ from typical propellers since their blades are mounted on a ring rotating within a slot in their nozzle, and their tips are oriented inwards, rather than outwards. Therefore, although some RDTs also have a hub, this is actually not required for the rotation of their blades, avoiding the onset of a large axial vortex in the wake of these propellers. This feature of RDTs is highly beneficial, since the hub vortex is the largest flow structure shed by conventional propellers, for instance, creating issues of unsteady interactions with downstream bodies, such as rudders, and producing vibrations and noise, in addition to erosion and structural damage.[2–5] Meanwhile, although RDTs work within a nozzle, unlike typical ducted propellers, there is no gap between their blades and the inner surface of the nozzle. This avoids the onset of cross-flows between the pressure and suction sides of the blades, where large turbulent stresses and strong pressure minima develop, with the potential inception of cavitation phenomena. Therefore, RDTs do not shed leakage vortices. Meanwhile, the presence of the gap between the rim moving the rotor blades and the statoric part of the propeller results in the onset of a parasitic torque, creating some penalty to the overall performance, but having little influence on the physics of the wake flow.[6–8]

Actually, RDTs are not a very recent idea,[9] but their practical implementation was made possible only in recent years, thanks to the development of compact, brushless electric motors, which can be installed within the stator (the nozzle) of these propellers. This is also the reason why the literature on RDTs is currently still quite limited, with most works focusing mainly on their global performance[6,10–29] and only a few studies reporting more details on their flow physics, such as their inner flow[7,8,30–32] and wake development.[33–36] However, during the last two decades, the wake of more conventional marine propellers was analyzed in detail,[37–51] because of its importance in the definition of the acoustic signature and interaction with rudders as well as for its rich flow physics, which makes its investigation of interest to both engineers and scientists. In agreement with the earlier theoretical study on helical vortex filaments by Widnall,[52] the experimental and numerical works on the dynamics of the wake of marine propellers demonstrated that their tip vortices undergo short and long waves

instabilities, leading eventually to mutual inductance between them and leapfrogging phenomena, resulting in vortex meandering and finally in the breakup into smaller structures, triggering a rise and following diffusion of turbulence levels. Moreover, the interaction occurring between the trailing wake of the blades and the tip vortices of the neighboring blades, due to their different pitch and thus their different velocity of downstream convection, was identified as an additional source of perturbation of the tip vortices, accelerating the disruption of the coherence of the flow structures populating the wake system.[53,54]

Among the several studies on the wake dynamics of marine propellers, a few of them have explored the influence of the number of blades on their streamwise development.[39,55,56] For conventional propellers, increasing blades numbers were found to accelerate their breakup, shifting the onset of mutual inductance and leapfrogging phenomena to upstream coordinates. This behavior was attributed to the diminishing azimuthal distance between trailing wakes, resulting in a faster shear of the tip vortices with the wake of the following blades and a stronger inductance between neighboring tip vortices. This phenomenon may be considered similar to that occurring for increasing loads.[53,57–60] They result in a smaller pitch of the wake of the propeller blades, producing shorter inter-spiral distances and a wider gap between the pitches of the tip vortices and trailing wake of each blade, which also leads to a faster interaction of the former with the trailing wakes of the following blades.

Similar investigations on the influence of the number of blades on the wake dynamics of RDTs are not available in the literature. The only exception is represented by the numerical study reported by Gaggero,[33] where detached eddy simulation (DES) on a computational mesh consisting of $44 \times 10^6$ finite volumes was adopted for the analysis of the wake flow of RDTs with four and six blades. However, in that work, the focus was on the comparison with the wake system of a ducted propeller operating within the same nozzle and producing the same thrust, as well as the comparison with the wake prediction by Reynolds-averaged Navier–Stokes (RANS) simulations. Meanwhile, the changes affecting the wake dynamics of RDTs are substantial, as demonstrated by Gaggero,[33] suggesting that the conclusions on the influence of the number of blades on the wake development of conventional propellers may not extend to their case. In particular, RDTs shed root vortices at their outermost radii as well as a shear layer from the trailing edge of their nozzle, instead of the typical tip vortices of conventional propellers. In addition, at the innermost radii, the wake of RDTs is populated by inner tip vortices, instead of the root vortices and the large hub vortex of typical propellers. In other words, in the particular case of RDTs, the wake is dramatically modified in comparison with that analyzed in the existing investigations on the subject.

In this study, large eddy simulation (LES) computations are reported for four RDTs, producing the same overall thrust, for the purpose of a fair comparison across them, but having blade numbers ranging from three to six. They are the result of an optimization study aimed at maximizing performance and minimizing cavitation inception for the given thrust.[14] We explore the influence of the number of blades of RDTs on the topology of the wake and its breakup process, as well as turbulence statistics. To the authors' knowledge, this is the first work on this subject, using an eddy-resolving methodology on a computational grid consisting of $6.3 \times 10^9$ points, which is a couple of orders of magnitude more extensive than in the most advanced DES studies currently available on the wake development of RDTs,[33–36] which typically utilize meshes of $O(10^7)$ finite volumes. This paper is organized in methodology (Sec. II), flow problem (Sec. III), computational setup (Sec. IV), analysis of the wake flow (Sec. V), and conclusions (Sec. VI).

## II. METHODOLOGY

In this study, the flow problem is governed by the filtered Navier–Stokes equations for incompressible flows, which in non-dimensional form are

$$\frac{\partial \tilde{u}_i}{\partial x_i} = 0, \tag{1}$$

$$\frac{\partial \tilde{u}_i}{\partial t} + \frac{\partial \tilde{u}_i \tilde{u}_j}{\partial x_j} = -\frac{\partial \tilde{p}}{\partial x_i} - \frac{\partial \tau_{ij}}{\partial x_j} + \frac{1}{Re}\frac{\partial^2 \tilde{u}_i}{\partial x_j^2} + f_i, \tag{2}$$

where the indexes $i$ and $j$ span the three directions in space, $t$ is time, $x_i$ and $x_j$ being the coordinates in the directions $i$ and $j$, $\tilde{u}_i$ and $\tilde{u}_j$ being the filtered velocity components in the directions $i$ and $j$, $\tilde{p}$ is the filtered pressure, $\tau_{ij}$ is the subgrid scale (SGS) stress tensor, $f_i$ is a forcing term, and $Re$ is the Reynolds number. This results from scaling the dimensional equations by using a reference length, $\mathscr{L}$, a reference velocity, $\mathscr{V}$, and the density of the fluid, $\rho$, and is defined as

$$Re = \frac{\mathscr{L}\mathscr{V}\rho}{\mu} = \frac{\mathscr{L}\mathscr{V}}{\nu}, \tag{3}$$

where $\mu$ and $\nu$ are the dynamic and kinematic viscosities of the fluid, respectively.

The SGS tensor, $\tau_{ij} = \widetilde{u_i u_j} - \tilde{u}_i \tilde{u}_j$, is the result of filtering the non-linear terms of the Navier–Stokes equations and represents the action of the unresolved scales on the resolved ones. This is typically modeled by using an eddy-viscosity hypothesis, based on Boussinesq's approximation, which assumes that the deviatoric part of the SGS tensor and the deformation tensor of the resolved velocity field, $\tilde{S}_{ij}$, are aligned

$$\tau_{ij}^d = \tau_{ij} - \frac{1}{3}\delta_{ij}\tau_{kk} = -2\nu_t \tilde{S}_{ij}, \tag{4}$$

where $\delta_{ij}$ is the Kronecker delta, $\tau_{kk}$ is the trace of the SGS tensor, and $\nu_t$ is the eddy-viscosity. This assumption reduces the number of unknowns of the problem of turbulence closure from the six independent elements of the symmetric tensor $\tau_{ij}$ to the only eddy-viscosity. This scalar needs to be modeled. In this study, the wall-adaptive local eddy-viscosity (WALE) model was adopted, which is discussed in detail by Nicoud and Ducros[61] and was successfully employed in several earlier works on marine propellers.[46,47,62–65] In particular, it has the convenient property of switching off in regions of pure strain (laminar gradients with no turbulence) and reproducing the correct limiting behavior of the eddy-viscosity in the vicinity of solid walls with no need for *ad hoc* corrections.

The forcing term $f_i$ in Eq. (2) was utilized to enforce the no-slip boundary conditions on solid walls by using an immersed boundary (IB) methodology, which decouples the discretization of the computational domain by the Eulerian grid, where the governing equations are resolved, from the discretization of the bodies immersed within the flow, represented by Lagrangian grids. Based on their position relative to the Lagrangian grids, the Eulerian points are separated into "fluid," "solid," and "interface." The interface points are those placed at the

boundary between the fluid and solid regions. In the particular implementation of the IB methodology adopted in the present computations, they are the points of the Eulerian grid placed outside the immersed boundaries, but having at least an interior (solid) neighbor in any coordinate direction of the Eulerian grid. All other points outside the immersed boundaries are tagged as fluid. Boundary conditions are enforced at the solid and interface points, while at the fluid points, velocity, pressure, and eddy-viscosity come from the solution of the equations governing the flow. At the solid points, the boundary condition is the velocity of the bodies where they are located, which may be stationary or moving. At the interface points, the velocity condition comes from a trilinear interpolation along the direction normal to the surface of the Lagrangian grid representing the particular immersed boundary. This local reconstruction utilizes, as boundary conditions, the no-slip requirement on the surface of the body as well as the velocities at the fluid points surrounding the particular interface point. Therefore, the term $f_i$ at the interface and solid points of the Eulerian grid in Eq. (2) is computed as

$$f_i = \frac{\mathscr{U}_i - \tilde{u}_i}{\Delta t} - \tilde{\mathscr{R}}_i, \tag{5}$$

where $i = 1, 2, 3$, $\mathscr{U}_i$ is the velocity boundary condition at the particular solid or interface point, $\tilde{u}_i$ is the filtered velocity at the same point from the previous time level, $\Delta t$ is the step of advancement in time of the numerical solution, while $\tilde{\mathscr{R}}_i$ is the sum of all convective, viscous, pressure gradient, and SGS terms of Eq. (2), all computed explicitly from the resolved (filtered) velocity, pressure and eddy-viscosity fields.

The governing equations were discretized in space on a staggered grid in cylindrical coordinates by using centered, second-order finite-differences. For Eq. (1), this resulted in a hepta-diagonal Poisson problem. This was decomposed into a penta-diagonal system of equations for each meridian slice of the grid by using trigonometric transformations along the periodic azimuthal direction. Each penta-diagonal system was efficiently inverted by means of a direct solver.[66] The advancement in time utilized a fractional-step technique.[67] The convective, viscous, and SGS terms of radial and axial derivatives in Eq. (2) were discretized by the explicit, three-step Runge–Kutta scheme. To relax the resolution requirements in time arising at the axis of the cylindrical grid, the terms of azimuthal derivatives were instead discretized by the implicit Crank–Nicolson scheme. This was actually also the case of the terms of radial derivatives in a particular region of the cylindrical grid (the root of the blades of the RDTs and the inner surface of their nozzle), where the radial spacing becomes very small, as discussed later in Sec. IV, where the Eulerian grid will be described in detail.

More details on the overall solver are reported in the works by Balaras[68] and Yang and Balaras,[69] where it was demonstrated to be second-order accurate in both space and time and where validations on canonical flow problems are reported. The same solver was also validated on several complex flows, including cases dealing with marine propellers.[46,47,62–65] It is also important to mention that in this section, the symbol $\sim$ was utilized to indicate filtered quantities. In Secs. IV and V, this notation will be omitted for convenience, since the whole analysis will deal with resolved quantities only. About this point, it is useful to mention that the modeled turbulent stresses were estimated to be of the order of 1% of the resolved ones, which means that the latter are a very good approximation of the total turbulent stresses.

## III. FLOW PROBLEM

Four propellers are considered in this study. They are RDTs, sharing the same geometry of the stator (the nozzle), with the exception of the streamwise extent of the slot for the rim, and differing in the number of blades of their rotors, but producing the same overall thrust. The number of blades ranges from three to six across the four geometries, which are represented in Fig. 1. These cases will be indicated hereafter as *RDT*3, *RDT*4, *RDT*5, and *RDT*6, respectively. They are the outcome of an earlier optimization study, aimed at maximizing the efficiency of propulsion and minimizing cavitation inception for the given thrust at the design working condition.[14] For the specific optimization problem, the design space consisted of 18 parameters, one constraint (thrust), and 8 objectives, including the efficiency of propulsion and seven different cavitation risk indicators on both suction and pressure sides of the blades. Each optimization process, dealing with a particular number of blades, was initialized with a population sampling quasi randomly the design space. The number of evolutions of this initial population was kept identical for all four blade numbers by using a metaheuristic (genetic) optimization algorithm. In general, this approach does not ensure uniform results across different design processes and the opportunity to select geometries having identical performance indicators relevant to cavitation inception across blade numbers. In the particular case, we may hypothesize that the optimization algorithm favored the shift of the load toward outer coordinates in the three-bladed case to keep high levels of efficiency (during the optimization process, while converging to the optimal design, the three-blades geometries experienced the lowest efficiency of propulsion, compared to the four-, five-, and six-blades configurations[14]). About this point, it is useful to recall that from inner to outer radii, the force generated on the blades contributes increasingly to the thrust it is able to produce and less to the torque required for its rotation. This is due to the increase in the tangential velocity, changing the angle of the velocity of the flow relative to the blade profile, and is beneficial to the efficiency of propulsion. This displacement of the load toward outer radii for *RDT*3 was also enabled by the larger value of the chord length for this particular geometry. This results in a smaller load per unit chordwise length, granting *RDT*3 the largest margins against suction side cavitation across all geometries.[14] In contrast, larger numbers of blades allowed a more uniform spanwise distribution of the lower load per blade, compared to the three-bladed case, especially at the outermost radii.

Therefore, as a result of this optimization process, the geometries of the propeller blades are not similar. This is shown in Fig. 2, where the evolution of the chord length, $c$, the pitch, $P$, and the maximum camber, $C$, are reported across the span of the propeller blades. In Fig. 2, $D$ is the rotor diameter. As expected, the average size of the chord length is diminishing from *RDT*3 to *RDT*6 in Fig. 2(a), since an increasing number of blades results in smaller blades required to produce the same overall thrust. However, it is interesting to notice the significant deviations in the radial distribution of the chord length for the geometry *RDT*3, if compared to all other cases. While the values of the chord length for *RDT*3 are similar to those characterizing the other geometries at the innermost radii, they become obviously larger at the outermost ones. Significant differences also affect the blade pitch in Fig. 2(b), which is monotonically growing from inner to outer radii for *RDT*3, in contrast with the case of *RDT*4, whose pitch distribution is rather uniform, while for *RDT*5 and *RDT*6 it is even decreasing. These

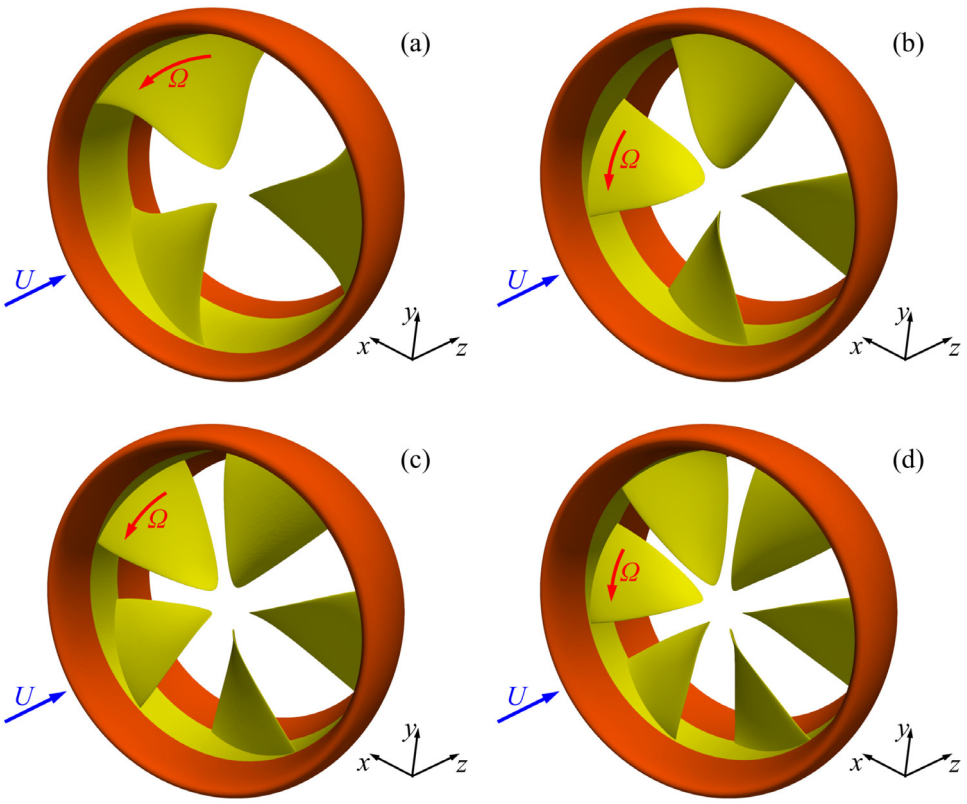


**FIG. 1.** Visualization of the four thrusters: (a) *RDT*3, (b) *RDT*4, (c) *RDT*5, and (d) *RDT*6. Yellow and orange colors for the rotors and the stators, respectively.

distributions are indicative of a blade geometry for *RDT*3 characterized by a more significant shift of the load from inner toward outer radii, if compared to the other cases. This is also confirmed by the maximum camber in Fig. 2(c). The implications of these differences will be clear when the fluid dynamics are analysed in Sec. V. The present comparison across the number of blades, although less straightforward, was considered more useful than just scaling the size of each blade, based on the thrust that each blade needs to produce, which is obviously inversely proportional to the number of blades. In this case, each geometry is the one producing the best efficiency of propulsion for the given thrust and the particular number of blades. All thrusters do not need a rotating hub, which is an important difference from conventional propellers, since they are moved by the rim rotating in a slot of the nozzle, thanks to an electric motor installed within the statoric part of the propulsion system.

The working conditions of marine propellers are typically characterized by means of the following quantities:

$$J = \frac{V}{nD}, \quad Re_{70\%R} = \frac{c_{70\%R}\sqrt{(2\pi n\, 0.7R)^2 + V^2}}{\nu_w}. \tag{6}$$

In Eq. (6), $J$ is called the advance coefficient, $V$ is the advance velocity, and $n$ is the frequency of rotation of the propeller blades. In this study, open-water conditions are considered, which means that all propellers operate alone within a uniform flow. Therefore, the advance velocity is equal to its free-stream value, $U$. $Re_{70\%R}$ is the Reynolds number at the reference radial location $r = 70\%R$, where $R = 0.5D$, $c_{70\%R}$ is the chord of the propeller blades at the same radial location, while $\nu_w$ is the viscosity of water. All thrusters were simulated at the advanced coefficient $J = 1.034$, which is the one for which their optimal design was found. The Reynolds number changes across cases since an increasing number of blades results in a decreasing size of each blade, having a smaller chord. Therefore, the model-scale Reynolds numbers considered in this study are $Re_{70\%R} \approx 332\,000$, $276\,000$, $265\,000$, $239\,000$ for *RDT*3, *RDT*4, *RDT*5, and *RDT*6, respectively.

## IV. COMPUTATIONAL SETUP

All simulations were conducted within a cylindrical domain ranging from $2.5D$ upstream and $5.0D$ downstream of the rotor's plane, where the origin of the streamwise coordinates was placed. The radial extent of the domain was equivalent to $5.0D$. Since open-water conditions were simulated, a uniform axial velocity was enforced at the inlet section, while at the outlet section, convective conditions were utilized for all three velocity components, using $U$ as convective velocity to transport away from the domain the eddies that otherwise cluster at the outlet boundary. These conditions were designed by Orlanski[70] in order for the flow structures to cross the boundary of the computational domain with minimal reflections, limiting the influence on the numerical solution of the flow to only a few grid cells. As discussed

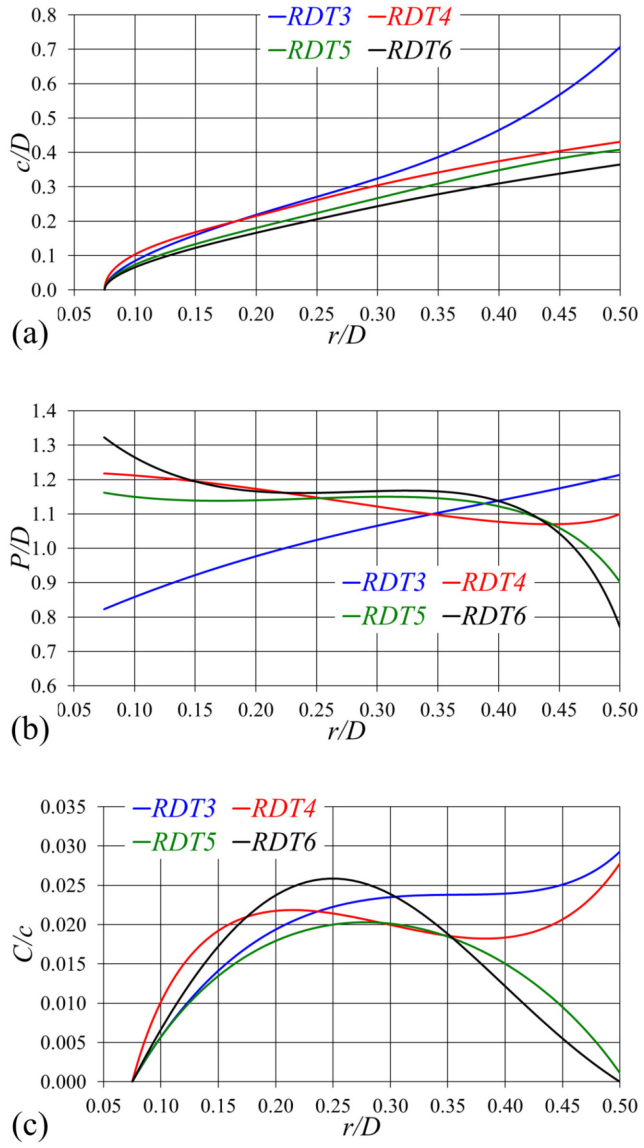


**FIG. 2.** Radial evolution of (a) the chord, $c$, (b) the pitch, $P$, and (c) the maximum camber, $C$, of the propeller blades: comparison across thrusters. $D$ is the diameter of the rotor.

also by Han *et al.*,[71] this strategy enables a significant contraction of the size of the computational domain. Free-stream conditions with impermeability were imposed at the cylindrical lateral boundary of the domain by setting $u = 0$, $\partial v/\partial r = 0$, and $\partial w/\partial r = 0$, where $u$, $v$, and $w$ are the instantaneous, resolved velocity components along the radial, azimuthal, and streamwise directions, respectively, while $r$ is the radial coordinate of the cylindrical reference frame. Homogeneous Neumann conditions were enforced for both pressure and eddy-viscosity at all external boundaries of the computational domain.

The angular azimuthal spacing of the grid, $\Delta\vartheta$, was uniform. Therefore, the cylindrical topology of the Eulerian grid utilized to discretize the computational domain allowed clustering points toward inner radial coordinates, where the propellers were placed, and the gradients of the solution were the highest. All geometries were simulated on an Eulerian grid consisting of $960 \times 2562 \times 2562$ $(6.3 \times 10^9)$ points along the radial, azimuthal, and axial directions, respectively. While the azimuthal spacing was uniform, as discussed above, the radial and axial resolutions were refined in the regions populated by the propellers and their wake. The radial grid was characterized by a uniform resolution of $\Delta r/D = 1.0 \times 10^{-3}$ across the span of the blades and the nozzle. However, this was refined up to $\Delta r/D = 5.0 \times 10^{-5}$ in the vicinity of the inner surface of the nozzle, in order to accurately resolve the root vortices produced at the intersection between the blades and the rim. The axial grid was also uniform across the rotor blades, where the maximum resolution was achieved, equivalent to $\Delta z/D = 5 \times 10^{-4}$, increasing smoothly downstream up to $z/D = 3.5$, with the purpose of resolving the wake structures. Further downstream coarsening was accelerated, up to the outflow boundary of the computational domain at $z/D = 5.0$. The most downstream region of the domain is indeed affected by the outflow boundary conditions. Therefore, we considered it unnecessary to keep high levels of streamwise resolution in that region. We verified that the near-wall resolution was equivalent to about 4, 6, and 8 wall-units in the normal, streamwise, and spanwise directions, respectively. Simplified representations of some slices of the Eulerian grid are reported in Fig. 3, where, for visibility of the grid lines, only a sample of points is shown. In the framework of the adopted IB methodology, while the Eulerian grid discussed above was utilized to discretize the computational domain, the discretization of the geometries of the propellers was achieved by using Lagrangian grids. The geometries of the rotors and the stators were represented by about 200 000 and 150 000 triangles for each case. They are visualized in Fig. 4.

It is important to mention that the case *RDT*4 was also simulated on coarser Eulerian grids to check the grid independence of the results. While the one discussed above will be indicated as "fine" grid, the "medium," and "coarse" grids were generated by increasing the spacing in all directions according to factors equal to $\sqrt[3]{2}$ and $\sqrt[3]{4}$. By using this strategy, the overall number of points of the computational grid was reduced by factors equal to 2 and 4, respectively, but keeping the same distribution of grid points along the radial and axial directions, while the azimuthal spacing was still uniform. Therefore, the "medium" and "coarse" grids consisted of $765 \times 2050 \times 2050$ $(3.2 \times 10^9)$ and $615 \times 1602 \times 1602$ $(1.6 \times 10^9)$ points, respectively.

Based on the discussion reported in Sec. II, the resolution in time of all simulations was tied to that in space by the stability requirements of the explicit, three-step Runge–Kutta scheme. Therefore, given the resolution in space, the resolution in time was very fine. All simulations were carried out enforcing a constant value of the Courant–Friedrichs–Lewy number equal to $CFL = 1.0$. As a result, each step of advancement in time was equivalent to rotations of 0.071°, 0.064°, 0.054°, and 0.063° for *RDT*3, *RDT*4, *RDT*5, and *RDT*6, respectively, which means that each revolution of the propellers required roughly 6000 time steps, in order to resolve the fastest dynamics of the smallest scales of the flow on the fine Eulerian grid. As expected, on the medium and coarse grids, the requirements of time resolution of the simulations of the *RDT*4 case were relaxed, resulting in a number of time steps per revolution equal to about 4300 and 3400, respectively.

All simulations were advanced in time during two flow-through times (15 time units, equivalent to about 15 revolutions) in order to

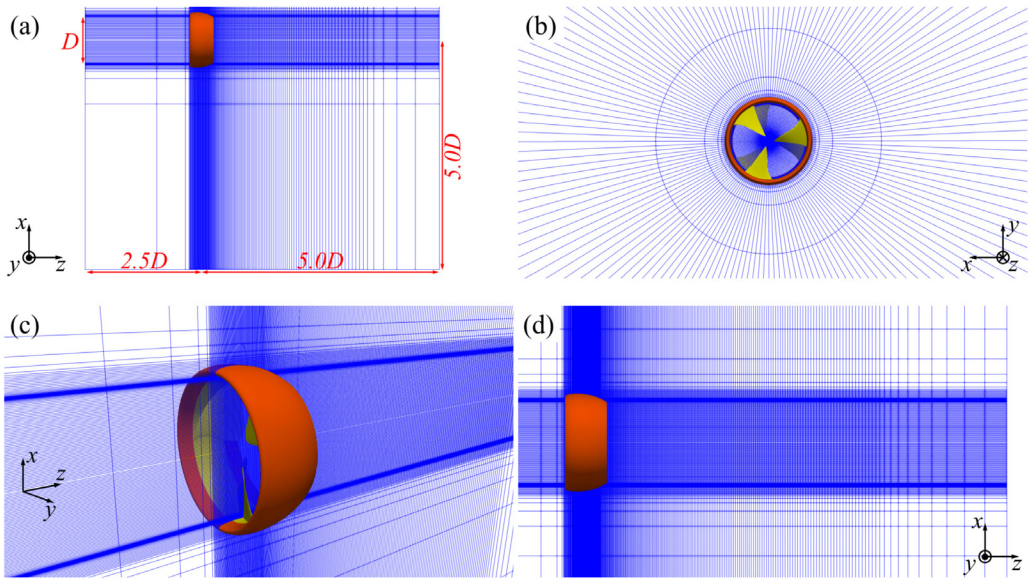


**FIG. 3.** Visualizations of the Eulerian grid dealing with (a) a meridian slice, (b) a cross-stream slice, (c) a detail of a meridian slice in the vicinity of the propeller, and (d) a detail of a meridian slice downstream of the propeller. For visibility of the grid lines, only one of every 256 and 64 points is shown in the top and bottom panels, respectively.

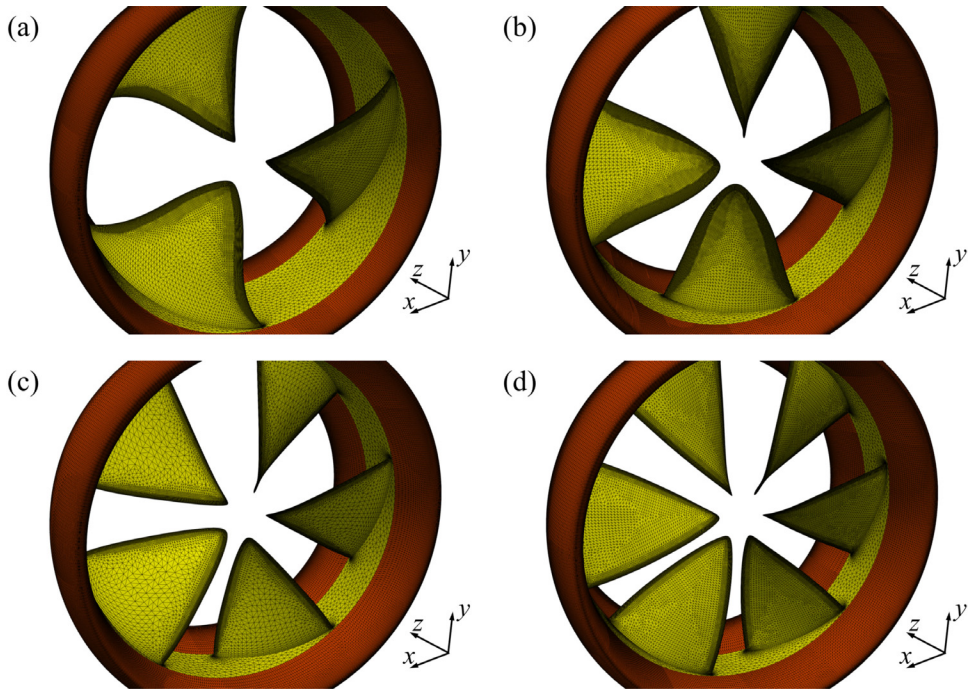


**FIG. 4.** Lagrangian grids of the (a) *RDT*3, (b) *RDT*4, (c) *RDT*5, and (d) *RDT*6 propellers.

develop statistically steady conditions in the wake. Then, both time-averaged and phase-averaged statistics were computed at run time during ten additional rotations, including within the statistical sample all realizations of the solution, consisting of about 60 000 instantaneous fields. The time-averages and phase-averages were computed within stationary and rotating reference frames, respectively, and will be denoted as $\overline{\varphi}$ and $\widehat{\varphi}$, where $\varphi$ is a generic physical quantity. The mean squares in time will be indicated as $\overline{\varphi'\varphi'}$ and $\widehat{\varphi'\varphi'}$ for the

time-averaged and phase-averaged statistics. In particular, the turbulent kinetic energy was computed from the mean squares of the three velocity components as

$$\overline{k} = \frac{1}{2}\left(\overline{u'u'} + \overline{v'v'} + \overline{w'w'}\right), \tag{7}$$

$$\widehat{k} = \frac{1}{2}\left(\widehat{u'u'} + \widehat{v'v'} + \widehat{w'w'}\right), \tag{8}$$

respectively for the time-averaged and phase-averaged statistics.

All simulations were carried out in a high-performance computing environment, by using a parallel in-house-developed Fortran solver with Message Passing Interface (MPI) capabilities, able to split the overall problem into smaller cylindrical subdomains, distributed across cores of the Leonardo DCGP cluster at CINECA, Italy. In particular, all computations on the fine grid were performed on 1280 cores, while those on the medium and coarse grids for *RDT*4 were distributed across 1024 and 800 cores. The overall computational cost of all simulations was equivalent to about $10 \times 10^6$ core hours.

## V. RESULTS

### A. Global performance

Although the major focus of the present study is the comparison of the wake development of RDTs across blade numbers, the global coefficients of performance are reported, mainly for comparison with the RANS simulations conducted on the same thrusters. Even if RANS is not well-suited for the analysis of the wake flow, it is accurate enough for the computation of the overall loads, especially at the design conditions considered in this study.[72–74] Note also that both LES and RANS simulations did not include in the computational model the effect of the gap flow produced in the small clearance between the rotor and the stator, which would have been computationally expensive, also due to the additional restrictions tied to numerical stability. The coefficients of performance are defined as follows:

$$K_T = \frac{T}{\rho n^2 D^4}, \quad K_Q = \frac{Q}{\rho n^2 D^5}, \quad \eta = \frac{JK_T}{2\pi K_Q}, \tag{9}$$

where $T$ and $Q$ are the thrust produced by the propeller and the torque required by its rotation, respectively. It should be noted that, while the contribution of the nozzle to the torque is negligible, this is not the case for the thrust. Therefore, $K_T$ is given by $K_T = K_{Ts} + K_{Tr}$, where $K_{Ts}$ and $K_{Tr}$ are the thrust coefficients of the stator (the nozzle) and the rotor (consisting of blades and rim), respectively. In particular, in this case, while the rotor generates a positive thrust, the nozzle produces a negative one. It is indeed a decelerating nozzle, whose purpose is to mitigate the peaks of negative pressure and the inception of cavitation phenomena, rather than to increase the overall thrust. However, about this point, it is important to mention that both RANS and LES computations considered in this study do not include a cavitation model. In the following, for confidentiality reasons, all results of performance will be scaled by reference values, which were taken as the coefficients $\overline{K}_T$, $\overline{K}_Q$, and $\overline{\eta}$ from the RANS computations on the *RDT*3 thruster. Note that all thrust coefficients were scaled by the overall $\overline{K}_T$ of *RDT*3, including both components attributable to the rotor and the stator, respectively. In Table I, the scaled values are denoted with a star, while the percentage deviations of each coefficient of performance from the RANS computations for each case are indicated by using the notation $\Delta\overline{\varphi}$. As discussed above, all geometries were designed to produce the same overall thrust, within a tolerance. Therefore, all values of $\overline{K}^*_T$ are close to 1.0. All geometries show similar values of efficiency of propulsion, and in general, no trend as a function of the number of blades can be observed. This is in line with the target of the optimization process in the earlier work by Gaggero,[14] aimed at finding the best geometry of the propeller blades, in terms of efficiency of propulsion, for each number of blades. The major purpose of the data in Table I is rather to demonstrate the close agreement with the results of the RANS computations, with relative errors well within 3%.

**TABLE I.** Time-averaged parameters of global performance from the LES computations on the fine grid, scaled by the values from the RANS computations in the *RDT*3 case. $\Delta\overline{\varphi}$ for the deviation from the RANS computation of each case.

| | *RDT*3 | *RDT*4 | *RDT*5 | *RDT*6 |
|---|---|---|---|---|
| $\overline{K}^*_{Tr}$ | 1.2463 | 1.2405 | 1.2551 | 1.2855 |
| $\Delta\overline{K}_{Tr}$ | +0.41% | −1.14% | −0.13% | +0.82% |
| $\overline{K}^*_{Ts}$ | −0.2435 | −0.2761 | −0.2687 | −0.2781 |
| $\Delta\overline{K}_{Ts}$ | −0.93% | −0.44% | +1.73% | +0.01% |
| $\overline{K}^*_{T}$ | 1.0028 | 0.9643 | 0.9865 | 1.0075 |
| $\Delta\overline{K}_{T}$ | +0.28% | −1.58% | +0.32% | +1.05% |
| $\overline{K}^*_{Q}$ | 0.9790 | 0.9577 | 0.9669 | 0.9702 |
| $\Delta\overline{K}_{Q}$ | −2.10% | +1.17% | +1.29% | −0.82% |
| $\overline{\eta}^*$ | 1.0243 | 1.0070 | 1.0203 | 1.0384 |
| $\Delta\overline{\eta}$ | +2.43% | −2.72% | −0.96% | +1.88% |

The data reported in Table I deal with the computations conducted on the fine grid. As discussed above, for the case *RDT*4, simulations on the medium and coarse grids were also carried out to assess the level of grid convergence of the results. The relevant data for the

**TABLE II.** Time-averaged parameters of global performance from the LES computations of the *RDT*4 case on the medium and coarse grids, scaled by the values from the RANS computations in the *RDT*3 case. $\Delta\overline{\varphi}$ for the deviation from the RANS computation of *RDT*4. $\delta\overline{\varphi}$ for the deviation from the LES computation of *RDT*4 on the fine grid.

| | Medium grid | Coarse grid |
|---|---|---|
| $\overline{K}^*_{Tr}$ | 1.2722 | 1.2479 |
| $\Delta\overline{K}_{Tr}$ | +1.40% | −0.54% |
| $\delta\overline{K}_{Tr}$ | +2.56% | +0.60% |
| $\overline{K}^*_{Ts}$ | −0.2753 | −0.2737 |
| $\Delta\overline{K}_{Ts}$ | −0.13% | +0.46% |
| $\delta\overline{K}_{Ts}$ | −0.31% | −0.90% |
| $\overline{K}^*_{T}$ | 0.9970 | 0.9742 |
| $\Delta\overline{K}_{T}$ | +1.75% | −0.57% |
| $\delta\overline{K}_{T}$ | +3.38% | +1.03% |
| $\overline{K}^*_{Q}$ | 0.9391 | 0.9152 |
| $\Delta\overline{K}_{Q}$ | −0.79% | −3.32% |
| $\delta\overline{K}_{Q}$ | −1.94% | −4.44% |
| $\overline{\eta}^*$ | 1.0616 | 1.0645 |
| $\Delta\overline{\eta}$ | +2.56% | +2.84% |
| $\delta\overline{\eta}$ | +5.43% | +5.72% |

parameters of global performance are reported in Table II, where the notation $\delta\overline{\varphi}$ was utilized to indicate the percentage variation of each coefficient of performance from the results of the LES simulation of *RDT*4, conducted on the fine grid. Overall, the grid dependence is small, with the highest errors affecting $\overline{\eta}$, since coarser grids overestimate the thrust coefficient and underestimate the torque coefficient, resulting in higher values of efficiency of propulsion, if compared to the results on the fine grid. However, the deviations from the RANS computation keep within a few percent, demonstrating that the coarser grids are also able to estimate quite accurately the coefficients of performance. The convergence of the thrust coefficient of the rotor is not monotonic, since the deviation from the result on the fine grid is larger on the medium grid than on the coarse grid. This may be due to the non-linear nature of the phenomena captured by the adopted eddy-resolving approach, as well as to the similarity of the parameters of performance across computational grids, with the results on the coarse grid already very close to those on the fine grid. This is not a surprising behavior in LES computations.[75,76]

### B. Wake structure

The results in Fig. 5 provide an overview of the wake topology by using the Q-criterion.[77] It is clear that the flow downstream of the thrusters consists of multiple helical vortices populating the trailing wake of the propeller blades across all geometries, in addition to the inner tip vortices and the outer root vortices. These vortices originate from the pressure side of the blades of each propeller as a result of cross-flow instabilities, promoted by centrifugal effects and observed also for conventional marine propellers in several earlier works.[62,64,78,79] However, also important differences from the fluid dynamics of the wake of conventional propellers are worth mentioning. The typical wake of marine propellers is dominated by the hub vortex at its axis and the tip vortices at its outer boundary. In contrast, the visualizations of Fig. 5 do not show any axial vortex, as expected, while the helical vortices populating the inner radii can be isolated to distances further downstream, if compared to the ones at the outer boundary of the wake, which experience a faster diffusion.

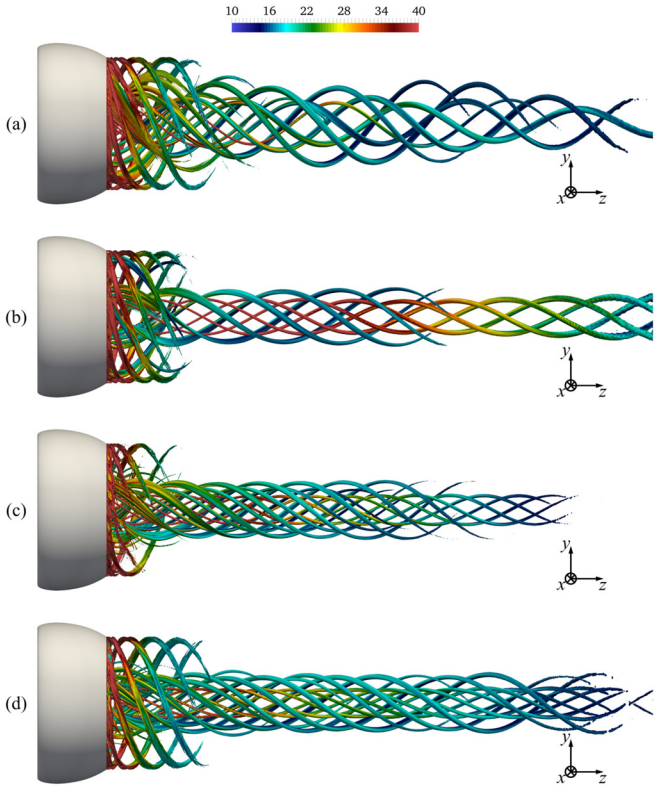


**FIG. 5.** Isosurfaces for (a) *RDT*3, (b) *RDT*4, (c) *RDT*5, and (d) *RDT*6, based on the Q-criterion from phase-averaged statistics of the solution ($QD^2/U^2 = 50$) and colored with the vorticity magnitude, scaled by $U/D$.

It is interesting to notice that merging events involving the helical vortices populating the trailing wake of each blade occur. They are better distinguishable in Fig. 6, where both geometries and isosurfaces were blanked out for $r/D > 0.42$, for visibility of the inner vortices of the wake core. Some particular merging phenomena are indicated by black arrows. Instead, events of mutual inductance between vortices from different blades were not observed, which is in contrast with the typical behavior of the tip vortices shed by conventional marine propellers.[39] As discussed in Sec. I, the literature on the wake system of conventional propellers identified mutual inductance and leapfrogging events as fundamental steps for the onset of the process of turbulent energy cascade from the tip vortices. These phenomena are not visible in the phase-averaged visualizations of Figs. 5 and 6 and were not observed in animations generated from instantaneous realizations of the solution, not reported here for limitation of space. All these behaviors are shared across geometries, hardly affected by the number of blades, and will be discussed in more detail below when the wake statistics are analysed. It is also worth mentioning that, although it may be possible that higher loads than design could promote more interactions of the innermost vortices, by increasing their intensity and decreasing their pitch, they appear more coherent across further downstream distances than the tip vortices of conventional propellers. This is especially the case, taking into account that their location at inner radii should actually result in a stronger mutual inductance by decreasing the distance between neighboring helices. For the same reason, an increasing number of blades should promote a stronger interaction by decreasing the azimuthal distance of the vortices from different blades, as observed for conventional propellers.[55] This was not the case in the present simulations, where increasing the number of blades did not trigger mutual inductance events.

It is also important to notice that the wakes of the four thrusters in Figs. 5 and 6 are not "similar," which is consistent with their design. It should be recalled that they were designed to optimize the efficiency of propulsion and minimize the risk of cavitation, resulting in an optimal distribution of the load for each blade number, different across cases. This means, for instance, that the load at the inner tip of the blades does not scale with their number. This is the reason why, although each blade of the *RDT*3 geometry is the most loaded across cases, less intense inner tip vortices are produced, in particular if compared to *RDT*4, which is the thruster shedding the most intense ones. Such a lower intensity of the inner tip vortices shed by the *RDT*3 propeller is revealed by the contours of vorticity magnitude in Figs. 5 and 6, achieving lower values in that case, especially if compared to those shed by *RDT*4. More details are also provided below by means of radial profiles of vorticity magnitude downstream of the rotor. This point is

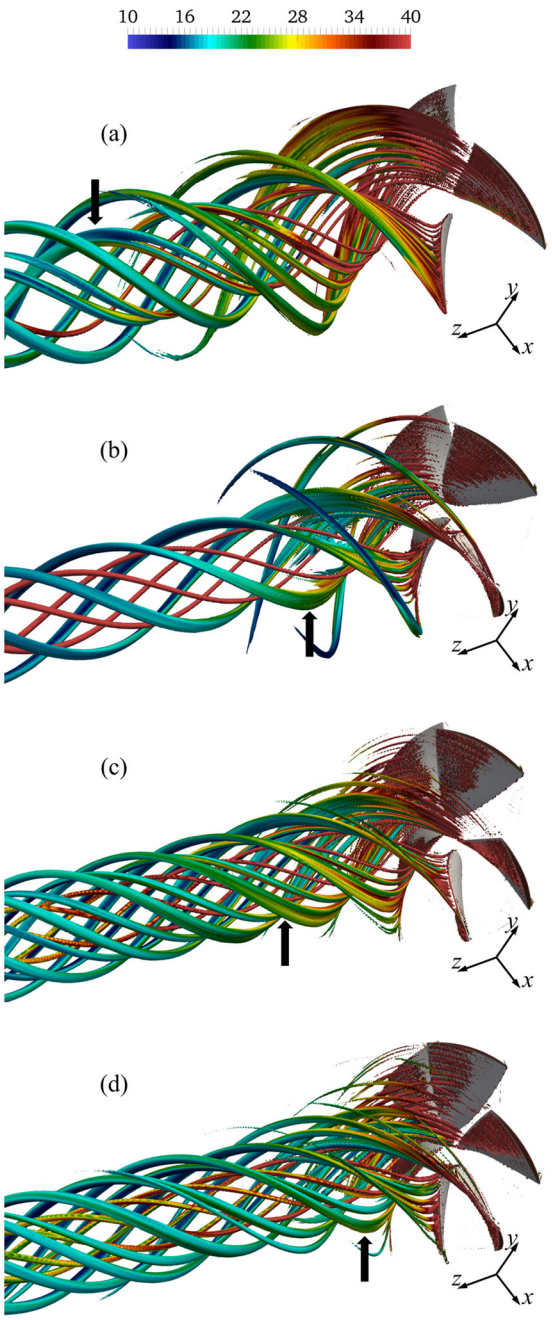


**FIG. 6.** Isosurfaces based on the Q-criterion for (a) *RDT*3, (b) *RDT*4, (c) *RDT*5, and (d) *RDT*6 from phase-averaged statistics of the solution ($QD^2/U^2 = 50$) and colored with the vorticity magnitude, scaled by $U/D$. Both geometries and isosurfaces blanked out for $r/D > 0.42$ for visibility of the wake core. Arrows indicate coupling events between helical vortices of the trailing wake of each blade.

clarified in Fig. 7, where the radial distribution of the force on the blades per unit spanwise length is represented. In Fig. 7(a), all values are scaled by $\bar{f}_{MAX}$, which is the peak value across all blades, that is, the one relative to *RDT*3, while in Fig. 7(b), they are scaled by $\bar{f}_{\max}$,

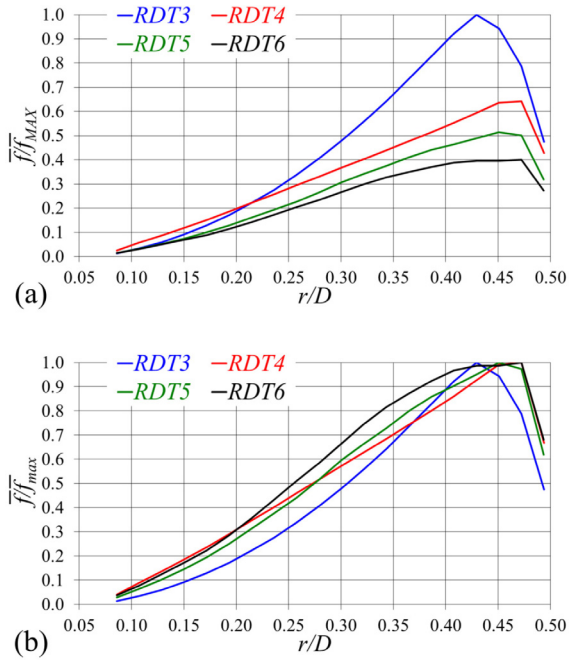


**FIG. 7.** Radial profiles of the force per unit spanwise length, $\bar{f}$, over the propeller blades, normalized by the peak value (a) across all cases, $\bar{f}_{MAX}$, and (b) for each case, $\bar{f}_{\max}$.

which is the peak value for each case. The visualizations in Fig. 7 highlight that, although the largest overall force is produced on the blades of *RDT*3, as expected, the largest values at the inner end of the blades occur for *RDT*4, which is the one shedding the most intense inner tip vortices. Figure 7(a) shows indeed that $\bar{f}/\bar{f}_{MAX}$ for $r/D < 0.20$ is actually larger for *RDT*4 than for *RDT*3. *RDT*3 is the case displaying the most significant shift of the overall load from inner toward outer radii, corresponding to the fastest radial growth of the forces over the blades and the most intense vortices shed at mid radial coordinates between the tip and the root of the blades. For instance, in Fig. 7(b), *RDT*3 starts from the lowest value of $\bar{f}/\bar{f}_{\max}$ across all cases at the innermost radii to the largest one at $r/D \approx 0.43$. It is also important to point out that the force represented in Fig. 7 consists mainly of azimuthal and axial components, generating torque and thrust. In other words, the overall force in Fig. 7 is contributing only in part to the generation of thrust. Therefore, its faster growth from inner toward outer radii for *RDT*3 is due not only to the smaller number of blades, but also to the differences across geometries in terms of pitch distribution, shown in Fig. 2(b), affecting the balance between azimuthal (torque-producing) and axial (thrust-producing) components of the overall force across the span of the blades.

Radial profiles of time-averaged vorticity magnitude at $z/D = 0.15$ are shown in Fig. 8. The arrows in Fig. 8(a) indicate the maxima relevant to the inner tip vortices and the outer root vortices. The latter are more intense than the former, since the load of the propeller blades grows from inner radii toward outer radii (see Fig. 7) and the lack of leakages and cross-flows allows keeping large loads even at the outermost radii of the propeller blades, in contrast with conventional propellers. While for the root vortices the intensity of the relevant maxima

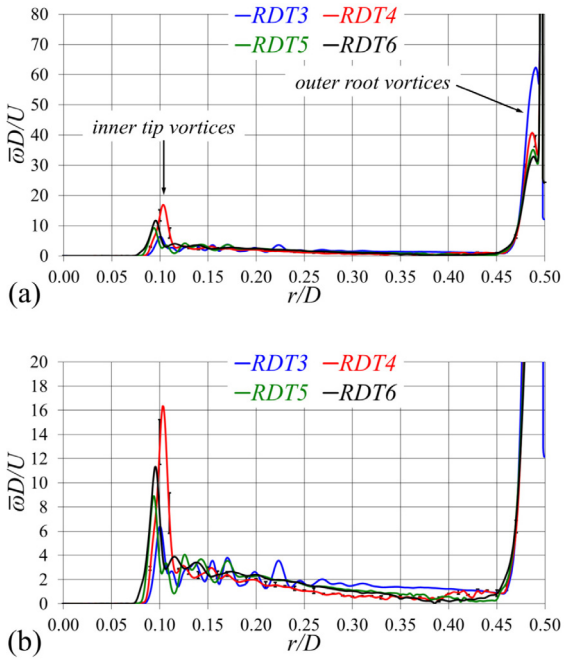


**FIG. 8.** Radial profiles of time-averaged vorticity magnitude at the streamwise location $z/D = 0.15$: different vertical scales in (a) and (b). Vertical bars for *RDT*4 indicate the grid uncertainty.

is a decreasing function of the number of blades, this is not the case for the inner tip vortices, as pointed out above. For instance, the highest inner peak is achieved in the case *RDT*4, while the lowest one is in the case *RDT*3, since the blades are not similar across thrusters and the intensity of the inner tip vortices does not scale with the number of blades. The detail of Fig. 8(b) is useful to highlight the presence of several local maxima at mid radial coordinates, representing the signature in the time-averaged statistics of the helical vortices populating the trailing wake of the propeller blades. The most intense ones are those downstream of *RDT*3. Although the blades of this thruster are the most loaded ones, this result is not obvious. In thrust similitude, it is obvious that the rotors with less blades are shedding more intense trailing wakes, characterized by higher levels of vorticity and turbulent stresses. This definitely affects the comparison across phase-averaged statistics. This is not the case for the time-averaged statistics, which are computed in a stationary reference frame. The frequency of the passage of the trailing wakes of the propeller blades at each Eulerian point of the computational grid is indeed the smallest for *RDT*3. This would balance in the time-averaged statistics the higher intensity of the flow structures shed by its blades, if they were similar to those of the other propellers, since all of them are producing the same overall thrust. However, as discussed above, the number of blades of the four thrusters was not changed across cases with the requirement of keeping them similar, but with the objective of maximizing the efficiency of propulsion and minimizing the risk of cavitation within the rotor for each number of blades. Therefore, the higher intensity of the local maxima at intermediate radii correlates with the lower intensity of the inner tip vortices for *RDT*3, since the overall load is more shifted away from the innermost radii toward mid radial coordinates, in comparison with the other

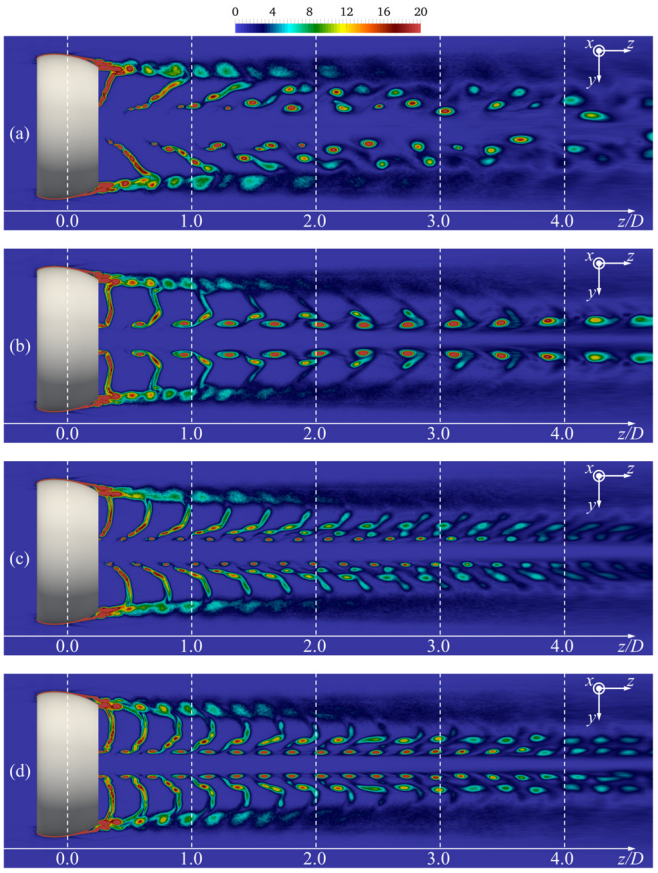


**FIG. 9.** Contours of vorticity magnitude on a meridian slice for (a) *RDT*3, (b) *RDT*4, (c) *RDT*5, and (d) *RDT*6 from phase-averaged statistics, scaled by $U/D$.

geometries. For the same reason, the lowest local maxima of vorticity at mid radii occur in the wake of *RDT*4, which is the thruster shedding the most intense inner tip vortices. Therefore, in general, for the same level of overall thrust, the lower the inner peak of vorticity of the time-averaged statistics tied to the tip vortices, the higher the local maxima within the wake core at mid radial coordinates.

The downstream evolution of the wake is shown through meridian slices in Fig. 9, providing additional evidence that the size of the vortices, whose signature is represented by local maxima of vorticity, grows at downstream coordinates, as a result of the merging of helical structures within the same trailing wakes. Again, the innermost vortices are the most coherent ones, while the outermost ones experience breakup into smaller scales, eventually undergoing diffusion, due to the shear produced at the outer boundary of the wake. These general features of the wake development are shared across all geometries, despite the changes affecting pitch and intensity of the wake structures. Note that the diffusion of the vorticity peaks accelerates downstream of $z/D = 3.5$, due to grid coarsening.

More details dealing with the comparison across geometries are given in Fig. 10, where radial profiles of time-averaged vorticity magnitude are shown at (a) $z/D = 0.5$ and (b) $z/D = 2.0$. If compared to the results in Fig. 8, the ones in Fig. 10 highlight that the several local maxima at mid radial coordinates are replaced by broader maxima

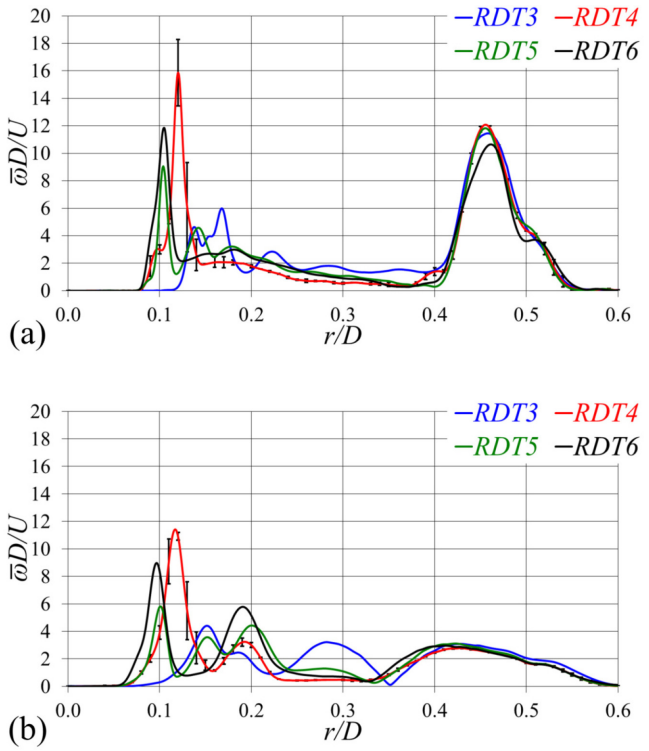


FIG. 10. Radial profiles of time-averaged vorticity magnitude at the streamwise locations (a) $z/D = 0.5$ and (b) $z/D = 2.0$. Vertical bars for *RDT*4 indicate the grid uncertainty.

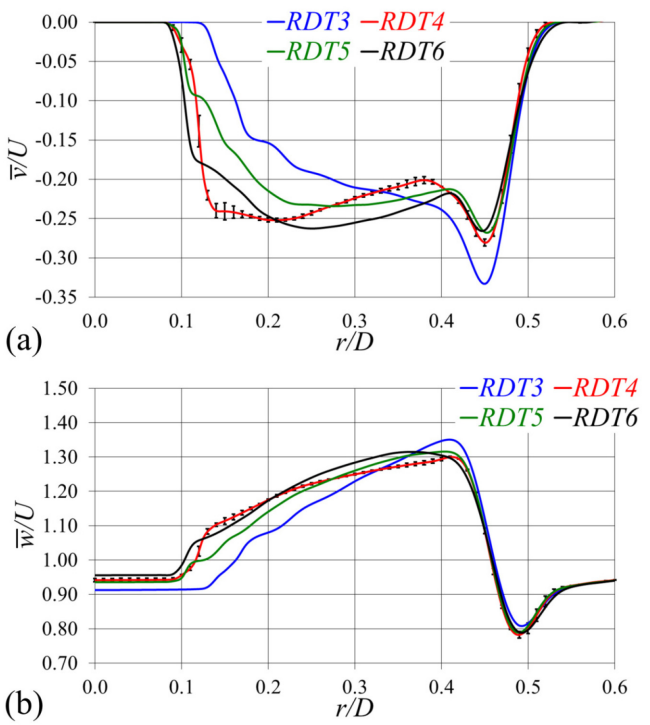


FIG. 11. Radial profiles of time-averaged (a) azimuthal velocity and (b) streamwise velocity at the streamwise location $z/D = 0.5$.

encompassing a wider radial extent of the wake, which is due to the merging phenomena across vortices, discussed above. For instance, the local peak at $r/D \approx 0.3$, for the case *RDT*3, experiences a growth in both intensity and radial extent from Figs. 10(a) and 10(b), despite the overall expected diffusion of the vorticity fields toward downstream coordinates. This increase is due to the overlapping effects of merging and outward radial shift of the helical vortices populating the trailing wake of the propeller blades. These phenomena are also visible, for example, at $r/D \approx 0.2$ for *RDT*4, *RDT*5, and *RDT*6. About the comparison across geometries, it is interesting to see again that the intensity of the vorticity values at mid radial coordinates is inversely proportional to the intensity of the inner tip vortices, since more intense inner tip vortices, originating from higher loads at the innermost radii, are equivalent to lower loads at mid radii and in turn weaker shear layers from the trailing edge of the propeller blades. Meanwhile, the vorticity peak at the boundary between the overall wake system and the free stream at $r/D \approx 0.45$, which is similar across cases, is the one experiencing the fastest downstream diffusion. This decay is due to the large shear produced at the outer boundary of the wake and is consistent with the quick breakup and diffusion of the wake structures at the outermost radial coordinates.

### C. Wake statistics

Radial profiles of time-averaged azimuthal and streamwise velocities are reported in Fig. 11 at $z/D = 0.5$. The shape of these profiles changes across cases, with those for *RDT*3 displaying the major deviations from the others. They feature the highest values of both velocity components at the outer boundary of the near wake. Meanwhile, *RDT*3 shows the lowest acceleration of the flow at the innermost radii, where the lowest values of azimuthal and streamwise velocities (in magnitude) are achieved across cases. This is in line with the radial distribution of the overall load across the propeller blades, which is the most shifted toward outer radial coordinates. In contrast, *RDT*4 is characterized by the most significant acceleration of the flow at the innermost radii. It is interesting to see that, in general, the largest radial gradients affect the outermost radii of the wake, where the flow accelerated by the propeller experiences shear with the surrounding free stream. These results can be explained by considering that, typically, the load on the blades of marine propellers is the highest at the outer radii, in order to achieve improved performance. This is even more the case of RDTs, which by design are more loaded than conventional propellers at the outermost radii, since there is no need of mitigating the intensity of the cross-flows between the pressure and suction sides of the blades and the resulting tip vortices. The importance of these points will become more clear in the following discussion.

The intense shear produced at the outer boundary of the wake is illustrated in Fig. 12 by means of contours of $\widehat{u'w'}$, which was found to be the most intense turbulent shear stress in the wake. It is interesting to see how the levels of shear achieved at inner radial coordinates are at least an order of magnitude lower than those within the shear layer of the nozzle across all cases, even at the core of the helical vortices within the trailing wakes of the propeller blades. This result is able to

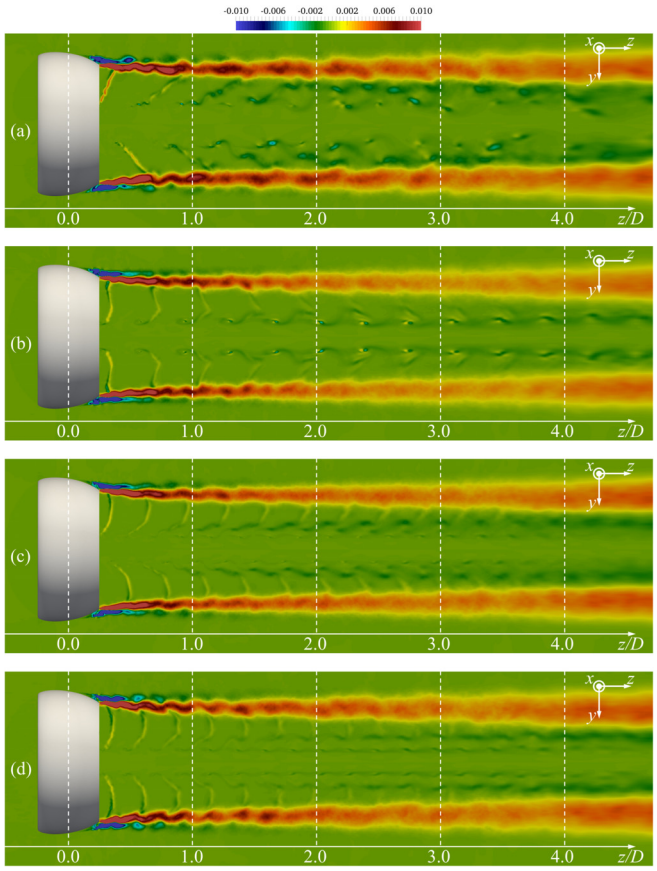


**FIG. 12.** Contours of the turbulent shear stress $\widehat{u'w'}/U^2$ on a meridian slice for (a) *RDT*3, (b) *RDT*4, (c) *RDT*5, and (d) *RDT*6 from phase-averaged statistics.

explain the faster breakup of the coherent structures populating the outer boundary of the wake, if compared to the inner ones. Although not reported here for the limitation of space, the same behavior was also found for the turbulent kinetic energy as well as the turbulent shear stresses $\widehat{u'v'}$ and $\widehat{v'w'}$, even if their levels were verified to be lower than those characterizing the turbulent shear stress $\widehat{u'w'}$. Once again, these results are shared across geometries, with no evident influence on them by the number of blades. In particular, for all cases, turbulence is mainly coming from the shear at the outer boundary of the wake and is not substantially influenced by the particular geometry and the increasing interaction between trailing wakes for increasing numbers of blades. As discussed above, the literature on conventional propellers often attributed the breakup of the tip vortices of conventional propellers to phenomena of shear with the wake of the following blades.[49,53,62,80] This shear is due to the smaller pitch of the tip vortices, if compared to the trailing wake of the blades. Therefore, as the wake system develops downstream, the trailing wake of each blade reaches the tip vortex of the preceding blade. These phenomena definitely occur also in the present case for the innermost helical structures, as shown in Fig. 9. Nonetheless, this interaction is not strong enough to produce a substantial rise in turbulence levels associated with the inner helical vortices, which were found coherent up to the outflow boundary of the computational domain or diffusion due to grid coarsening at the most downstream coordinates.

A more detailed comparison across cases is given in Fig. 13 for the time-averaged turbulent kinetic energy and the three turbulent shear stresses in the cylindrical reference frame at the streamwise coordinate $z/D = 0.5$. They are the highest for *RDT*3 across most radial coordinates. However, as discussed above, this is not the one producing the most intense inner tip vortices, which are those shed by *RDT*4, corresponding to the maxima in Fig. 13 at the innermost radial coordinates of the wake. Meanwhile, the most intense turbulent stresses occur at the outer boundary of the wake and are the highest for *RDT*3. This is also the case at mid radial coordinates. It is also worth noting again that this result is not obvious in the time-averaged statistics and is not a direct consequence of the smaller number of blades of *RDT*3. Although the blades of *RDT*3 are the most loaded ones, having to produce the same overall thrust as in the other cases with more blades, and thus their trailing wakes are characterized by the most intense shear layers, the time-averaged statistics also take into account the more frequent passage of the trailing wake of the propeller blades in the cases with more blades. This explains why at mid radii the levels of turbulent kinetic energy are similar across *RDT*4, *RDT*5 and *RDT*6, despite the different blade numbers, while for *RDT*6 they are even higher at the outermost radii. The highest values are achieved for all turbulent stresses in the wake of *RDT*3, especially at the outer boundary of the wake, since this is the case characterized by the most significant shift of the blades' load from inner toward outer radii. As discussed in Sec. III, this shift is tied to the need of keeping high levels of efficiency of propulsion with the requirement of producing a higher load per blade, in comparison with the other geometries.

The comparison across cases on the streamwise evolution of the turbulent stresses is given in Fig. 14, where all values were averaged across the radial region $0.0 < r/D < 0.6$ at each streamwise coordinate. Note that for the shear stresses, their magnitude was considered in order to avoid mutual cancelation between positive and negative values in the averaging process over cross sections. All results agree that the levels of turbulence are the highest downstream of *RDT*3 through the whole near wake, but an evident trend as a function of the number of blades is not revealed. The deviations across the other cases are indeed quite small, with the exception of a short distance downstream of the *RDT*6 propeller, where its values are higher than for *RDT*4 and *RDT*5. In Fig. 14(d), $\overline{v'w'}$ is higher for *RDT*4 than for *RDT*5 and *RDT*6 in the range of streamwise coordinates $0.5 < z/D < 2.0$, although this is the lowest across all turbulent stresses. Overall, the lowest turbulence levels are produced downstream of *RDT*5.

## VI. CONCLUSIONS

This study reported results on the wake flow of RDTs reproduced by using an LES approach on a cylindrical grid consisting of $6.3 \times 10^9$ points. Four geometries were analyzed, with different numbers of blades, designed in the framework of an optimization process to achieve the best efficiency of propulsion for a given thrust.[14] All cases were found to share the following similarities, independent of the number of blades:

- All wake systems were characterized by a faster diffusion of the helical vortices at outer radii, in comparison with those at the wake core, due to the large stresses produced at the outer boundary of the wake, populated by the shear layer shed from the

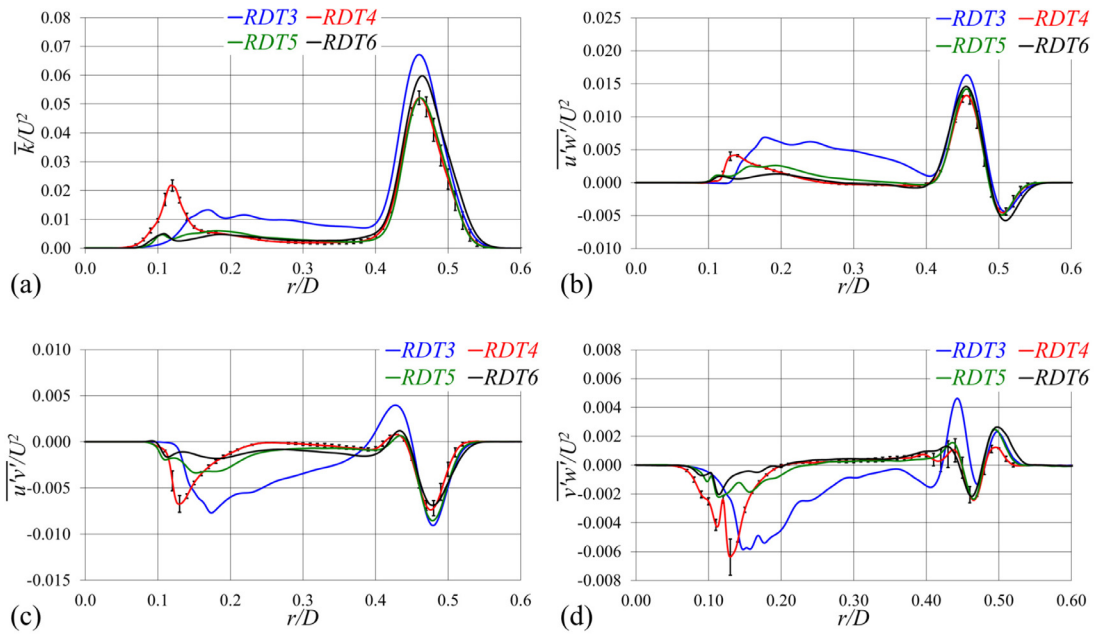


**FIG. 13.** Radial profiles of (a) $\overline{k}/U^2$, (b) $\overline{u'w'}/U^2$, (c) $\overline{u'v'}/U^2$, and (d) $\overline{v'w'}/U^2$ at the streamwise location $z/D = 0.5$. Vertical bars for *RDT4* indicate the grid uncertainty.

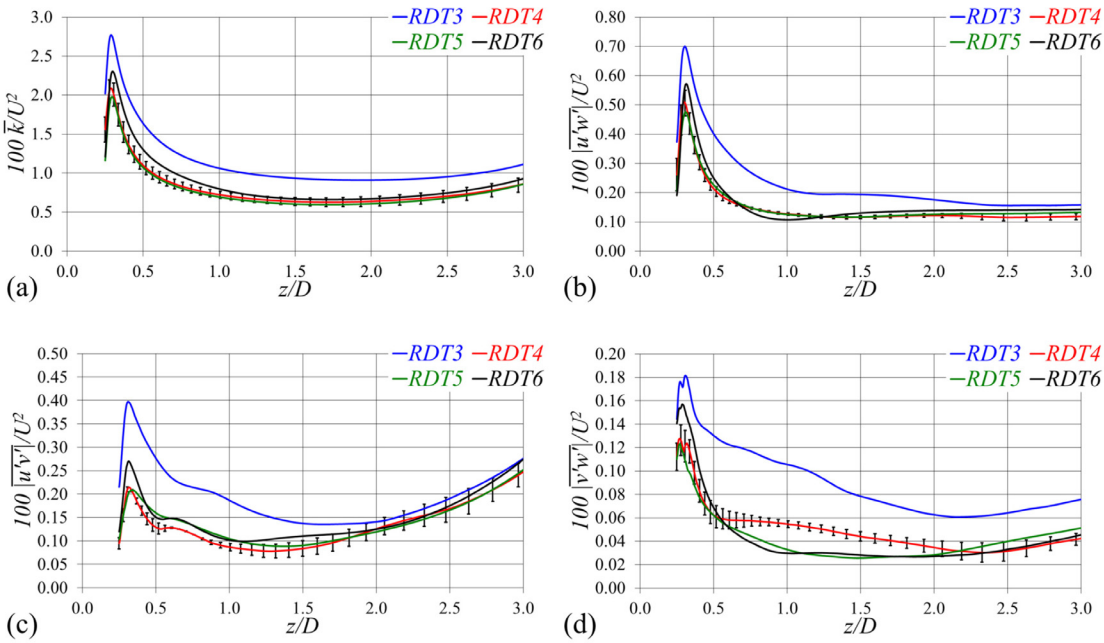


**FIG. 14.** Streamwise evolution of (a) $\overline{k}/U^2$, (b) $|\overline{u'w'}|/U^2$, (c) $|\overline{u'v'}|/U^2$, and (d) $|\overline{v'w'}|/U^2$. At each streamwise location average within the region $0.0 < r/D < 0.6$. Vertical bars for *RDT4* indicate the grid uncertainty.

trailing edge of the nozzle. As a result, while the wake of conventional propellers is characterized by tip vortices at its outer boundary and a large hub vortex at its axis, the wake of RDTs was found populated by smaller helical structures, especially at the innermost radii of the wake core.

- The interaction across the helical vortices of the trailing wake of each blade did not give rise to their break-up into smaller structures. In contrast, they merged into larger structures, as demonstrated by the onset of wider peaks of vorticity as the propeller wake developed downstream.

- In contrast with the typical wake system of conventional propellers, mutual inductance phenomena between vortices shed by different blades were not observed, at least within the simulated extent of the downstream flow and for the particular working condition. This was also the case of the inner tip vortices, despite their shorter mutual distance, if compared to the outer tip vortices of conventional propellers.

Referring to the last point, the comparison across geometries did not reveal, in contrast with the findings of earlier studies on the wake system of conventional propellers,[39,55,56] an increase in the mutual inductance phenomena and, in turn, a faster disruption of the coherence of the wake system for an increasing number of blades. In the literature on conventional propellers, this trend was attributed to the faster interaction of the tip vortices with the trailing wake of the following blades, which was hypothesized to be one of the major players in the process.[49,53,62,80] In this study, this interaction was not found to produce a faster breakup into turbulence of the inner tip vortices. This result is consistent with the finding that downstream of these propellers the most significant source of turbulent stresses is the shear at the outer boundary of the wake, rather than the interaction between the wake systems of different blades at the innermost radii. This difference from conventional propellers in terms of the influence of the number of blades on the wake dynamics may be due to two major reasons. (i) The tip vortices of conventional propellers are usually more intense, since for improved efficiency, the load over the propeller blades typically grows from inner toward outer radial coordinates. Therefore, more intense tip vortices are able to produce more intense mutual inductance events between each other. (ii) The outer tip vortices of conventional propellers experience more significant disturbances, due to their shear with the free stream, in comparison with the inner vortices of RDTs. These disturbances also make them more sensitive to the reinforced interactions due to larger numbers of blades.

The comparison across RDTs demonstrated that the highest time-averaged turbulent stresses were produced in the wake of the *RDT*3 geometry, with small differences across the other cases. As discussed above, the larger number of blades did not result in a significantly stronger shear between the closer tip vortices and trailing wakes of neighboring blades, which would have caused larger turbulent stresses. Meanwhile, the highest turbulent stresses were produced at the outer boundary of the wake, especially for *RDT*3. This was the geometry characterized by the most significant shift of the overall load toward outer radial coordinates, due to the need of producing the same overall thrust while keeping a satisfactory efficiency of propulsion.

As discussed above, the highest turbulent stresses were found in the shear layer at the outer boundary of the wake. Although a rigorous stability analysis[81,82] of this shear layer is beyond the scope of the present work, the instability phenomena which characterize this region of the wake of RDTs could be modeled as a Taylor–Couette–Poiseuille type of flow. Extensive details about this subject can be found in the work by Lueptow *et al.*[83] They studied experimentally the flow generated by concentric cylinders with the inner one in rotation and the presence of a streamwise pressure gradient, resembling in some way the conditions generated in RDTs. More recent studies on the instabilities of this class of flows can be found in the works by Heaton and Peake[84] and Suzuki.[85] In particular, Suzuki[85] utilized data from improved delayed DES to investigate the instability modes in the interstage flow between the rotor and the stator of a turbofan, especially in view of their impact on the relevant acoustic emission. Meanwhile, it is worth mentioning that the setup of the experiments by Lueptow *et al.*[83] may be considered only a rough approximation of the flow conditions in the wake of actual RDTs. For instance, the inner cylinder, represented by the rim of the rotor, is actually rotating within a slot of the outer nozzle, covering only part of its streamwise extent. The flow within this gap is not actually influencing the wake development. Furthermore, the shear layer shed by the nozzle is developing under the additional influence of the root vortices produced by the interaction of the boundary layer on the rim with the root of the propeller blades. Instead, the same approximation as in Lueptow *et al.*[83] could be more suitable to analyze the flow conditions generated in the gap region between the rim and the nozzle. This gap was not modeled in the present study because of its computational challenge and its negligible influence on the wake dynamics, as we verified by specific RANS computations on the same propellers. However, the phenomena occurring in that region have the drawback of generating a parasitic torque and, in turn, a penalty to the performance of propulsion. This is definitely a subject of interest for future studies.

## ACKNOWLEDGMENTS

The authors acknowledge EuroHPC JU for awarding the project EHPC-EXT-2024E02-066 access to Leonardo DCGP at CINECA in the framework of an extreme scale access call.

## AUTHOR DECLARATIONS

### Conflict of Interest

The authors have no conflicts to disclose.

### Author Contributions

**Antonio Posa:** Conceptualization (lead); Data curation (lead); Formal analysis (lead); Investigation (lead); Methodology (lead); Project administration (lead); Resources (lead); Software (lead); Validation (lead); Visualization (lead); Writing – original draft (lead); Writing – review & editing (lead). **Stefano Gaggero:** Conceptualization (supporting); Data curation (supporting); Formal analysis (supporting); Investigation (supporting); Methodology (supporting); Resources (supporting); Validation (supporting); Visualization (supporting); Writing – review & editing (supporting). **Riccardo Broglia:** Conceptualization (supporting); Methodology (supporting); Resources (supporting); Writing – review & editing (supporting).

## DATA AVAILABILITY

The data that support the findings of this study are available from the corresponding author upon reasonable request.

## REFERENCES

[1]X. Yan, X. Liang, W. Ouyang, Z. Liu, B. Liu, and J. Lan, "A review of progress and applications of ship shaft-less rim-driven thrusters," Ocean Eng. **144**, 142–156 (2017).
[2]W. Zhang, C. Chen, Z. Wang, Y. Li, H. Guo, J. Hu, H. Li, and C. Guo, "Numerical simulation of structural response during propeller-rudder interaction," Eng. Appl. Comput. Fluid Mech. **15**, 584–612 (2021).

[3]W. Zhang, F. Li, J. Ma, X. Ning, S. Sun, and Y. Hu, "Fluid-structure interaction analysis of the rudder vibrations in propeller wake," Ocean Eng. **265**, 112673 (2022).
[4]W.-S. Jang, W.-S. Choi, H.-G. Choi, S.-Y. Hong, and J.-H. Song, "Fatigue damage prediction of ship rudders under vortex-induced vibration using orthonormal modal FSI analysis," Mar. Struct. **88**, 103376 (2023).
[5]A. Posa, R. Broglia, E. Balaras, and M. Felli, "The acoustic signature of a propeller–hydrofoil system in the far field," Phys. Fluids **35**, 075101 (2023).
[6]P. Li, H.-D. Yao, C. Wang, and K. Weng, "Improved efficiency with concave cavities on S3 surface of a rim-driven thruster," Phys. Fluids **35**, 107102 (2023).
[7]J. Lin, H.-D. Yao, C. Wang, Y. Su, and C. Yang, "Hydrodynamic performance of a rim-driven thruster improved with gap geometry adjustment," Eng. Appl. Comput. Fluid Mech. **17**, 2183902 (2023).
[8]B. Cai, Q. Xu, B. Tian, L. Qiu, W. Chai, J. Qi, and L. He, "Improvement of the efficiency for rim-driven thrusters through acceleration of gap flow," Ocean Eng. **291**, 116480 (2024).
[9]H. E. Saunders, *Hydrodynamics in Ship Design* (Society of Naval Architects and Marine Engineers, New York, 1957).
[10]A. Yakovlev, M. Sokolov, and N. Marinich, "Numerical design and experimental verification of a rim-driven thruster," in Proceedings of the Second International Symposium on Marine Propulsion, Hamburg, Germany, 2011.
[11]Q.-M. Cao, F.-W. Hong, D.-H. Tang, F.-L. Hu, and L.-Z. Lu, "Prediction of loading distribution and hydrodynamic measurements for propeller blades in a rim driven thruster," J. Hydrodyn. **24**, 50–57 (2012).
[12]A. J. Dubas, N. Bressloff, and S. Sharkh, "Numerical modelling of rotor-stator interaction in rim driven thrusters," Ocean Eng. **106**, 281–288 (2015).
[13]B.-W. Song, Y.-J. Wang, and W.-L. Tian, "Open water performance comparison between hub-type and hubless rim driven thrusters based on CFD method," Ocean Eng. **103**, 55–63 (2015).
[14]S. Gaggero, "Numerical design of a RIM-driven thruster using a RANS-based optimization approach," Appl. Ocean Res. **94**, 101941 (2020).
[15]B. Liu and M. Vanierschot, "Numerical study of the hydrodynamic characteristics comparison between a ducted propeller and a rim-driven thruster," Appl. Sci. **11**, 4919 (2021).
[16]B. Cai, B. Tian, L. Qiu, Q. Xu, X. Mao, W. He, and W. Chai, "Application of the body force method in the rim driven thruster," Int. J. Naval Archit. Ocean Eng. **14**, 100476 (2022).
[17]H. Jiang, W. Ouyang, C. Sheng, J. Lan, and R. Bucknall, "Numerical investigation on hydrodynamic performance of a novel shaftless rim-driven counter-rotating thruster considering gap fluid," Appl. Ocean Res. **118**, 102967 (2022).
[18]L. Liu, W. Jiang, Z. Liu, R. Yu, and T. Bian, "Multi-objective optimization of shaftless rim-driven thruster based on ISIGHT," J. Phys.: Conf. Ser. **2369**, 012023 (2022).
[19]S. Zhai, S. Jin, J. Chen, Z. Liu, and X. Song, "CFD-based multi-objective optimization of the duct for a rim-driven thruster," Ocean Eng. **264**, 112467 (2022).
[20]C.-W. Chen, X.-P. Chen, Z.-Y. Zhou, C. Zhang, J. Chen, and T. Zheng, "The effect of tip rake distribution on the hydrodynamic performance of shaftless rim-driven contra-rotating thruster," Ocean Eng. **285**, 115454 (2023).
[21]B. Liu, M. Vanierschot, and F. Buysschaert, "Optimization design of the duct of a rim-driven thruster using the adjoint approach," Ocean Eng. **278**, 114293 (2023).
[22]B. Liu, M. Vanierschot, and F. Buysschaert, "Numerical study of scale effects on the open water performance of a rim-driven thruster," Appl. Ocean Res. **138**, 103667 (2023).
[23]B. Liu, M. Dai, and X. Liang, "Influence of bearings on the open water performance of a rim-driven thruster," Phys. Fluids **35**, 085139 (2023).
[24]Y. Nie, W. Ouyang, Z. Zhang, G. Li, and R. Zheng, "Multi-parameter optimization analysis of hydrodynamic performance for rim-driven thruster," Energies **16**, 891 (2023).
[25]Z. Wu, J. Gong, J. Ding, Y. Sun, and C. Ma, "Autonomous modification and optimization method for rim-driven system in surface ships," Ocean Eng. **290**, 116293 (2023).
[26]M. Lackner, A. Löhr, F. Schill, and M. Van Essche, "Rim driven thruster as innovative propulsion element for dual phase flows in plug flow reactors," Fluids **9**, 168 (2024).
[27]B. Liu, W. Ouyang, X. Yan, and M. Vanierschot, "Numerical investigation of hydrodynamic characteristics of a rim-driven thruster coupled with an underwater vehicle," J. Mar. Sci. Eng. **12**, 1838 (2024).
[28]B. Tao, L. Liangliang, C. Wenhao, J. Wen, and L. Zhiwen, "Multi-objective optimization design of shaftless rim-driven thruster," Proc. Inst. Mech. Eng., Part M **238**, 633–639 (2024).
[29]W. Ouyang, Z. Zhang, Y. Nie, B. Liu, and M. Vanierschot, "Parametric modeling and collaborative optimization of a rim-driven thruster considering propeller-duct interactions," Ocean Eng. **337**, 121746 (2025).
[30]Z. Zhu and H. Liu, "The external characteristics and inner flow research of rim-driven thruster," Adv. Mech. Eng. **14**, 16878132221081608 (2022).
[31]B. Liu, M. Vanierschot, and F. Buysschaert, "Effects of transition turbulence modeling on the hydrodynamic performance prediction of a rim-driven thruster under different duct designs," Ocean Eng. **256**, 111142 (2022).
[32]P. Li, C. Sun, H.-D. Yao, Z. Wang, C. Wang, and K. Weng, "The effects of domain division types on the performance prediction of a rim-driven thruster," Ocean Eng. **287**, 115809 (2023).
[33]S. Gaggero, "A study on the wake evolution of a set of RIM-driven thrusters," J. Mar. Sci. Eng. **11**, 1659 (2023).
[34]B. Liu, X. Yan, W. Ouyang, and M. Vanierschot, "Comparison study of the vortical structures in the wake of a rim-driven thruster and a ducted propeller in bollard conditions," Ocean Eng. **306**, 118064 (2024).
[35]C. Yang, H.-D. Yao, C. Sun, C. Wang, C. Guo, and J. Lin, "Numerical study of relationships between flows and structural characteristics of the rotor in a rim-driven hubless thruster using a strongly-coupling FSI algorithm," Ocean Eng. **323**, 120560 (2025).
[36]Z. Zhang, B. Liu, W. Ouyang, R. Zheng, and M. Vanierschot, "Analysis of the energy loss mechanism of a rim-driven thruster under open water conditions," Ocean Eng. **319**, 120203 (2025).
[37]B.-G. Paik, J. Kim, Y.-H. Park, K.-S. Kim, and K.-K. Yu, "Analysis of wake behind a rotating propeller using PIV technique in a cavitation tunnel," Ocean Eng. **34**, 594–604 (2007).
[38]M. Liefvendahl, "Investigation of propeller wake instability using LES," Ship Technol. Res. **57**, 100–106 (2010).
[39]M. Felli, R. Camussi, and F. Di Felice, "Mechanisms of evolution of the propeller wake in the transition and far fields," J. Fluid Mech. **682**, 5–53 (2011).
[40]P. Kumar and K. Mahesh, "Large eddy simulation of propeller wake instabilities," J. Fluid Mech. **814**, 361–396 (2017).
[41]M. Felli and M. Falchi, "Propeller wake evolution mechanisms in oblique flow conditions," J. Fluid Mech. **845**, 520–559 (2018).
[42]M. Cianferra, A. Petronio, and V. Armenio, "Non-linear noise from a ship propeller in open sea condition," Ocean Eng. **191**, 106474 (2019).
[43]S. Ahmed, P. Croaker, and C. J. Doolan, "On the instability mechanisms of ship propeller wakes," Ocean Eng. **213**, 107609 (2020).
[44]M. Cianferra and V. Armenio, "Scaling properties of the Ffowcs-Williams and Hawkings equation for complex acoustic source close to a free surface," J. Fluid Mech. **927**, A2 (2021).
[45]L. Wang, T. Wu, J. Gong, and Y. Yang, "Numerical simulation of the wake instabilities of a propeller," Phys. Fluids **33**, 125125 (2021).
[46]A. Posa, R. Broglia, and E. Balaras, "The dynamics of the tip and hub vortices shed by a propeller: Eulerian and Lagrangian approaches," Comput. Fluids **236**, 105313 (2022).
[47]A. Posa, "Dependence of tip and hub vortices shed by a propeller with winglets on its load conditions," Phys. Fluids **34**, 105107 (2022).
[48]H. Shi, T. Wang, M. Zhao, and Q. Zhang, "Modal analysis of non-ducted and ducted propeller wake under axis flow," Phys. Fluids **34**, 055128 (2022).
[49]C. Wang, P. Li, C. Guo, L. Wang, and S. Sun, "Numerical research on the instabilities of CLT propeller wake," Ocean Eng. **243**, 110305 (2022).
[50]K. Kan, H. Li, and Z. Yang, "Large eddy simulation of turbulent wake flow around a marine propeller under the influence of incident waves," Phys. Fluids **35**, 055124 (2023).
[51]L. Wang, X. Liu, J. Guo, M. Li, and J. Liao, "The dynamic characteristics in the wake systems of a propeller operating under different loading conditions," Ocean Eng. **286**, 115518 (2023).
[52]S. E. Widnall, "The stability of a helical vortex filament," J. Fluid Mech. **54**, 641–663 (1972).

[53]F. Di Felice, D. Di Florio, M. Felli, and G. Romano, "Experimental investigation of the propeller wake at different loading conditions by particle image velocimetry," J. Ship Res. **48**, 168–190 (2004).
[54]M. Felli, F. Di Felice, G. Guj, and R. Camussi, "Analysis of the propeller wake evolution by pressure and velocity phase measurements," Exp. Fluids **41**, 441–451 (2006).
[55]M. Felli, G. Guj, and R. Camussi, "Effect of the number of blades on propeller wake evolution," Exp. Fluids **44**, 409–418 (2008).
[56]J. Gong, J. Ding, and L. Wang, "Propeller-duct interaction on the wake dynamics of a ducted propeller," Phys. Fluids **33**, 074102 (2021).
[57]D.-G. Baek, H.-S. Yoon, J.-H. Jung, K.-S. Kim, and B.-G. Paik, "Effects of the advance ratio on the evolution of a propeller wake," Comput. Fluids **118**, 32–43 (2015).
[58]L. Wang, X. Liu, N. Wang, and M. Li, "Modal analysis of propeller wakes under different loading conditions," Phys. Fluids **34**, 065136 (2022).
[59]C. Wang, P. Li, Y. Han, and L. Hao, "The study on the wake of a CLT propeller under different advance coefficients," Appl. Ocean Res. **118**, 102996 (2022).
[60]T. Wu, Z. Wang, P. Hu, and W. Luo, "Tip vortex merging dynamics governing wake coherence evolution in marine propellers through advance coefficient modulation," Phys. Fluids **37**, 075115 (2025).
[61]F. Nicoud and F. Ducros, "Subgrid-scale stress modelling based on the square of the velocity gradient tensor," Flow, Turbul. Combust. **62**, 183–200 (1999).
[62]A. Posa, R. Broglia, M. Felli, M. Falchi, and E. Balaras, "Characterization of the wake of a submarine propeller via large-eddy simulation," Comput. Fluids **184**, 138–152 (2019).
[63]A. Posa, A. Capone, F. Alves Pereira, F. Di Felice, and R. Broglia, "Interaction between the helical vortices shed by contra-rotating propellers," Phys. Fluids **36**, 055116 (2024).
[64]A. Posa and R. Broglia, "Comparison between the wake systems of conventional and ducted propellers," J. Fluid Mech. **1011**, A15 (2025).
[65]A. Posa, A. Capone, F. Alves Pereira, F. Di Felice, and R. Broglia, "Comparison of performance and wake systems between conventional and contra-rotating propellers in thrust similitude," Phys. Fluids **37**, 065151 (2025).
[66]T. Rossi and J. Toivanen, "Parallel fast direct solver for block tridiagonal systems with separable matrices of arbitrary dimension," SIAM J. Sci. Comput. **20**, 1778–1796 (1999).
[67]J. Van Kan, "A second-order accurate pressure-correction scheme for viscous incompressible flow," SIAM J. Sci. Stat. Comput. **7**, 870–891 (1986).
[68]E. Balaras, "Modeling complex boundaries using an external force field on fixed Cartesian grids in large-eddy simulations," Comput. Fluids **33**, 375–404 (2004).
[69]J. Yang and E. Balaras, "An embedded-boundary formulation for large-eddy simulation of turbulent flows interacting with moving boundaries," J. Comput. Phys. **215**, 12–40 (2006).
[70]I. Orlanski, "A simple boundary condition for unbounded hyperbolic flows," J. Comput. Phys. **21**, 251–269 (1976).
[71]T. Han, J. Meng, and G. Innis, "An open boundary condition for incompressible stratified flows," J. Comput. Phys. **49**, 276–297 (1983).
[72]D.-Q. Li, "Validation of RANS predictions of open water performance of a highly skewed propeller with experiments," J. Hydrodyn. **18**, 520–528 (2006).
[73]M. Morgut and E. Nobile, "Influence of grid type and turbulence model on the numerical prediction of the flow around marine propellers working in uniform inflow," Ocean Eng. **42**, 26–34 (2012).
[74]R. Muscari, A. Di Mascio, and R. Verzicco, "Modeling of vortex dynamics in the wake of a marine propeller," Comput. Fluids **73**, 65–79 (2013).
[75]J. Meyers and P. Sagaut, "Is plane-channel flow a friendly case for the testing of large-eddy simulation subgrid-scale models?," Phys. Fluids **19**, 048105 (2007).
[76]M. Xiao, A. Ceci, P. Costa, J. Larsson, and S. Pirozzoli, "CaLES: A GPU-accelerated solver for large-eddy simulation of wall-bounded flows," Comput. Phys. Commun. **310**, 109546 (2025).
[77]J. Jeong and F. Hussain, "On the identification of a vortex," J. Fluid Mech. **285**, 69–94 (1995).
[78]Z. Jing and A. Ducoin, "Direct numerical simulation and stability analysis of the transitional boundary layer on a marine propeller blade," Phys. Fluids **32**, 124102 (2020).
[79]B. Boudenne and A. Ducoin, "Characterization of the transitional boundary layer flow on a marine propeller blade through under-resolved direct numerical simulation," Ocean Eng. **292**, 116631 (2024).
[80]S. Gaggero and M. Ferrando, "Wake instabilities of tip-loaded propellers: Comparison between CLT and &new generation' CLT configurations," J. Mar. Sci. Eng. **11**, 112 (2023).
[81]D. Crighton and M. Gaster, "Stability of slowly diverging jet flow," J. Fluid Mech. **77**, 397–413 (1976).
[82]P. Huerre and P. A. Monkewitz, "Local and global instabilities in spatially developing flows," Annu. Rev. Fluid Mech. **22**, 473–537 (1990).
[83]R. M. Lueptow, A. Docter, and K. Min, "Stability of axial flow in an annulus with a rotating inner cylinder," Phys. Fluids A **4**, 2446–2455 (1992).
[84]C. Heaton and N. Peake, "Algebraic and exponential instability of inviscid swirling flow," J. Fluid Mech. **565**, 279–318 (2006).
[85]T. Suzuki, "Spiral flow instability between a rotor and a stator in high-speed turbomachinery and its relation to fan noise," J. Fluid Mech. **966**, A1 (2023).